Simulation analysis of fracture process of slag deposits surrounding wall tubes during steam sootblowing[*]

Lin-tao SHAO[1], Jian-ping KUANG[2], Wei-juan YANG[†‡1], Yu ZHANG[2],

Zhi-jun ZHOU[1], Zhi-wen XIA[2], Zhi-hua WANG[1]

[1]State Key Laboratory of Clean Energy Utilization, Zhejiang University, Hangzhou 310027, China
[2]Ningxia Shenyao Science and Technology Co., Ltd, Yinchuan 750000, China
[†]E-mail: yangwj@zju.edu.cn
Received Jan. 24, 2019; Revision accepted Apr. 22, 2019; Crosschecked Apr. 24, 2019

Abstract: The slag deposited on the wall tubes of furnaces/boilers seriously reduces the heat transfer from the furnace to tubes and degrades the tubes by corrosion. During boiler operation, slag deposits are removed by sootblowers that blast the deposits with steam or air jets. In this study, we develop a novel numerical model using the cohesive zone method (CZM) and coupled Eulerian–Lagrangian (CEL) analysis to investigate the dynamics and mechanism of deposit fracture during sootblowing. Cohesive elements subject to the softening traction–separation relationship and evolution laws are embedded into the deposit model to describe crack formation during deposit breaking. The deposit cracking status is evaluated by extracting the scalar stiffness degradation variable from damaged cohesive elements. The dynamic process and mechanism of deposit fracture are analyzed and revealed in detail, particularly in terms of the destructive degree and fracture rate of the deposit model. The effects of the sootblowing steam pressure (0.9–1.8 MPa) on slag breaking, wall tube stress, and steam consumption are also investigated. Sootblowing steam pressures over 1.2 MPa do not further benefit the sootblowing effect but adversely affect the wall tube lifetime.

Key words: Sootblowing; Boiler; Numerical model; Cohesive zone method (CZM); Deposit fracture
https://doi.org/10.1631/jzus.A1900030   **CLC number:** TQ53

1 Introduction

The accumulation of fireside deposits can be a problem in boilers all over the world (Fan et al., 2001). Slag deposits on water wall tubes not only reduce the heat transfer efficiency in boilers but also degrade steam tubes by corrosion (Žbogar et al., 2006). Soot-blowing is an effective and conventional method to overcome this problem, and it can be performed using high-pressure steam, air, or sound waves. Deposit fracture caused by sootblowing is a complex mechanical process that includes the aerodynamic aspects of the sootblower jet and the breaking of the slag layer.

Previous studies at the University of Toronto, Canada (Jameel et al., 1994; Kaliazine et al., 1997, 1999) discussed sootblower jet dynamics and solid deposit removal mechanics. The effects of the deposit strength and thickness and sootblower jet characteristics on deposit removal were also investigated. In this regard, Pophali et al. (2009, 2013) used gypsum to simulate brittle deposits. They also performed many lab-scale experiments in which cylindrical gypsum deposits were exposed to a supersonic air jet. They obtained fundamental information on soot-blower jet dynamics and the interactions between the sootblower jet and the deposits. The results showed

that brittle deposits could be destroyed within a short blowing time (nearly 3 ms). Moreover, they developed a computational fluid dynamics model to predict the flow behavior of sootblower jets (Bussmann et al., 2013; Doroudi et al., 2014).

However, replicating the actual process of deposit failure through experiments is difficult due to the complexity of accurate observation of the furnace environment and slag properties. Coal ash deposits are usually assumed as brittle materials, which can be fractured by a sootblower jet (Ebrahimi-Sabet, 2001). With rapid developments and innovations in computer-aided engineering technology in recent years, several methods such as the finite element method (FEM) have been increasingly applied to replicate the process of brittle material breaking. Furthermore, the cohesive zone method (CZM) has been used extensively in predicting the fracture behavior of brittle materials. In this regard, Guo (2014) investigated a 3D fracture model through a combined finite-discrete element method and cohesive crack model. The author also discussed the sensitivity of mesh size and orientation to numerical results in another study (Guo et al., 2016). Jiang and Meng (2018) developed a 3D numerical model of rock breaking using a hybrid finite and cohesive element method to stimulate rock fracture and chip formation. Yao (2012) developed a 3D pore pressure CZM to predict crack initiation and growth in quasi-brittle materials considering the material softening effect. The author subsequently applied the model to predict hydraulic fracturing under fluid injection. Gálvez et al. (2002) presented a numerical procedure for mixed-mode fracture of quasi-brittle materials, whose mode is based on the cohesive crack approach. Their numerical results agreed relatively well with two experimental sets of mixed-mode fractures of concrete beams. Elices et al. (2002) indicated that the CZM could adequately predict the behavior of uncracked structures. This model, which was initially applied to concrete and cementitious composites, can also be successfully used for other materials such as polymer and certain steels.

In summary, numerical fracture models based on the CZM of brittle materials such as rock, ceramics, gypsum, and concrete have been generally developed and applied. The results of numerical fracture models based on the CZM have presented good agreements with experiments in the literature (Turon et al., 2007; Awinda et al., 2016; Gui et al., 2016; Jiang and Meng,

2018). However, this new simulation method has not thus far been applied to study ash deposit fracture in coal-fired boilers; previous studies have usually experimentally discussed the overall results of ash deposit removal by sootblowing. To replicate the ash deposit failure dynamically and comprehensively, we develop a novel 3D numerical model that combines the CZM and coupled Eulerian–Lagrangian (CEL) analysis in this study, and we consider all aspects of interest including ash deposit, wall tube, and sootblowing steam in the simulations. This new simulation study can contribute to a better understanding of the dynamics and detailed characteristics of the ash deposit fracture process, which have not been revealed thus far by experiments. The dynamic process of deposit fracture is revealed in detail, and the diffusion of the steam jet and spread of the stress wave in deposits are also analyzed. The sootblowing steam pressure is investigated to discover its effects on slag breaking, wall tube stress, and steam consumption.

2 Methods

2.1 CZM approach

The CZM in ABAQUS FE software adopted in this study is based on the model developed by Hillerborg et al. (1976). Cohesive elements can simulate several types of behavior at interfaces when the interface load-carrying capability is lost (Chen et al., 2009). The available traction–separation model in this approach initially assumes linear elastic behavior with nominal stress and strain quantities, followed by the evolution of damage. The typical traction–separation responsible for a single mode is defined by two points for the normal direction, that is, the onset of damage (δ_n^o, t_n^o) and complete decohesion $(\delta_n^f, 0)$ (May, 2015), as shown in Fig. 1, where t_s and t_t represent the shear components of traction, and δ_s and δ_t are the shear components of separation. The relative displacement at damage initiation, δ_n^o, for the normal direction is expressed as

$$\delta_n^o = \frac{t_n^o}{K_n}, \tag{1}$$

where t_n^o denotes the stress at initiation, and K_n is the element stiffness.

With the application of the maximum nominal stress criterion in this study, damage is assumed to be initiated when the maximum nominal strain ration reaches a value of 1 (Awinda et al., 2016). This criterion can be represented as

$$\max\left\{\frac{\langle t_n\rangle}{t_n^o}, \frac{t_s}{t_s^o}, \frac{t_t}{t_t^o}\right\} = 1, \qquad (2)$$

where $\langle\rangle$ represents the Macaulay bracket with the usual interpretation. These brackets are used to signify that a pure compressive deformation or stress state does not initiate damage. Therefore, $\langle t_n\rangle = t_n$ when $t_n > 0$; otherwise, $\langle t_n\rangle = 0$.

Damage evolution describes the rate of degraded material stiffness once the initiation criteria are met. In addition, zero normal and shear stiffnesses exist when the interface is fully destroyed under tension or full fracture opening (Gui et al., 2015). Scalar stiffness degradation variable D is proposed to represent the overall damage. This variable can also evolve from 0 to 1 with further loading after damage initiation (Jiang and Meng, 2018). Parameter D can be presented as follows for the normal direction (Camanho and Dávila, 2002; Kazerani et al., 2012):

$$t = \begin{cases} K\delta_n, & \delta_n \le \delta_n^o, \\ (1-D)K\delta_n, & \delta_n^o < \delta_n < \delta_n^f, \\ 0, & \delta_n \ge \delta_n^f, \end{cases} \qquad (3)$$

$$D = \frac{\delta_n^f(\delta_n - \delta_n^o)}{\delta_n(\delta_n^f - \delta_n^o)}, \quad \text{and} \quad 0 \le D \le 1, \qquad (4)$$

where K denotes the stiffness that relates the nominal stress to the displacement in CZM. D denotes an essential and a necessary variable to measure the extent of deposit failure in our study, and its meaning in the traction–separation curve is depicted in Fig. 1. Parameter δ^f denotes the displacement among adjoining elements when the material completely fails. This variable is defined on the basis of Griffith's theory (Griffith, 1921), which assumes that fracture energy G^f is absorbed during the formation of the fracture surface. Parameter G^f denotes a material property that corresponds to the shaded area under the traction–displacement curve in Fig. 1. In addition, fracture energy G^f can be expressed as (Guo, 2014)

$$G^f = \int_{\delta^o}^{\delta^f} t\,\mathrm{d}\delta \approx \frac{1}{3}t^o\delta^f. \qquad (5)$$

Therefore, failure displacement δ^f can be defined as

$$\delta^f = 3\frac{G^f}{t^o}. \qquad (6)$$
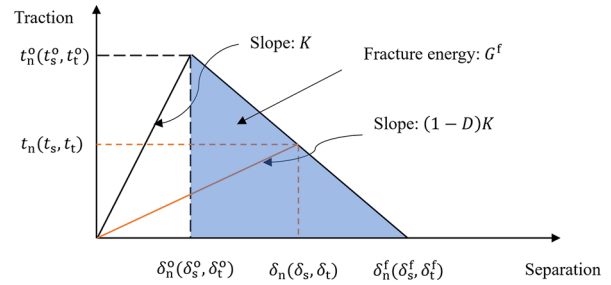
Fig. 1 Typical traction–separation response and damage response in cohesive zone method (CZM)

2.2 CEL analysis method

CEL is an effective method to solve unstable fluid–structure coupling surface problems, and it allows immediate transfer of the parameters between Eulerian and Lagrangian domains. This coupled approach can achieve the interaction of Eulerian and Lagrangian bodies within a model domain in ABAQUS. Thus, it is convenient to observe the dynamic process of steam-flow-coupled deposit fracture at the same time.

In the traditional Lagrangian analysis, nodes are fixed within the material, and the elements deform with the material. Lagrangian elements are consistently 100% full of a single material. Thus, the material boundary coincides with an element boundary. The deposit and wall tube model are based on Lagrangian analysis in this study. In contrast, in Eulerian analysis, the nodes are fixed in space, and materials flow through elements that do not deform. Eulerian elements may not consistently be 100% full of a single material. Therefore, the Eulerian material boundary must be computed during each time increment, and it does not correspond to an element boundary. If any Eulerian material moves outside the Eulerian mesh, then the material is lost from the simulation (ABAQUS, 2016). The high-temperature steam component is based on the Eulerian analysis in this study.

Fig. 2 presents the diagrammatic sketch of the entire CEL model including the Eulerian and Lagrangian regions. We first construct a cuboid Eulerian domain (meshed by Eulerian elements) containing all Lagrangian parts (meshed by Lagrangian elements including the deposit, wall tube, and jet). In the Eulerian domain, material assignment relies on the parameter of material volume fraction that is in the range of 0–1.0. The material volume fraction represents the percentage of the element's volume that is occupied by the given Eulerian material. A fraction value of 1.0 indicates that the region is completely filled with the Eulerian material (ABAQUS, 2016). In our simulation, the initial Eulerian material, steam, was assigned originally inside the jet nozzle (inner red region), and the volume fraction was zero in the Eulerian domain except in the inner red region. During the CEL analysis, the Eulerian material (sootblowing steam) was pressed and ejected from the nozzle continuously, and subsequently, ABAQUS tracked the Eulerian material in each element via calculating the volume fractions. When the Eulerian material interacted with the Lagrangian material (ash deposit), the stress on the deposit caused by steam impact was calculated according to the penalty method, which is the Eulerian–Lagrangian contact method in ABAQUS.

3 Numerical model and analysis

3.1 Cohesive zone modeling procedure

To realize the CZM approach, a certain type of element (i.e. cohesive elements with softening traction–separation relationship) and evolution laws were implemented among the solid elements in the initial mesh to model potential cracks (Su et al., 2010a, 2010b). In Fig. 3, two adjacent hexahedral elements (Fig. 3a) are considered as examples to clarify the procedure of embedding a zero-thickness eight-node cohesive element. The shared interface (i.e., nodes 1, 2, 3, and 4) between both adjacent hexahedral elements (① and ②) is replaced by an eight-node cohesive element (added new nodes 1′, 2′, 3′, and 4′) with zero thickness, as shown in Fig. 3b. Fig. 3c shows the detailed structure of the eight-node cohesive element. Such cohesive elements (element type: COH3D8) were automatically inserted into the deposit model

(element type: C3D8R) by a Python program. The C3D8R element was an eight-node linear brick with reduced integration and hourglass control, and this element type could prevent locking phenomena due to the reduced integration in ABAQUS. Note that linear elements should be chosen instead of quadratic elements, because the lumped mass method used with the linear elements is more effective in simulating the stress wave propagation than the consistent mass method used with the quadratic elements (ABAQUS, 2016).
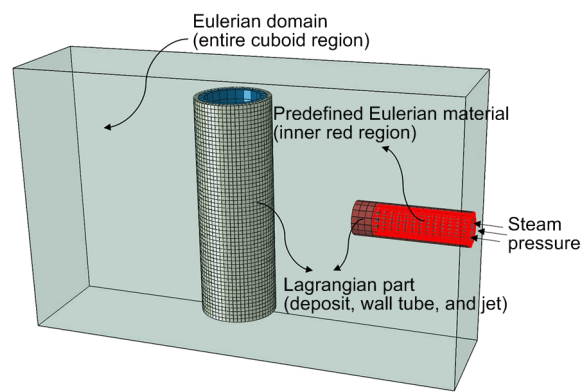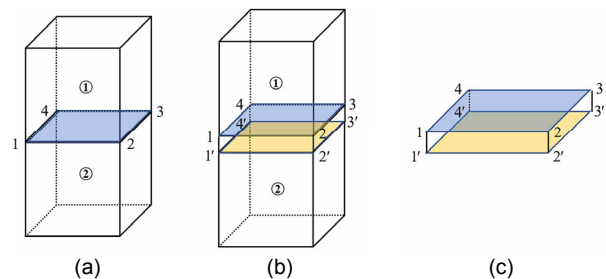

Fig. 2 Diagrammatic sketch of the entire CEL model
Note: for interpretation of the references to color in this figure, the reader is referred to the web version of this article

Fig. 3 Schematic of insertion of eight-node cohesive element between two hexahedral elements
(a) Two adjacent hexahedral elements; (b) Insertion of eight-node cohesive element; (c) Detailed structure of the cohesive element

3.2 Modeling of deposit and sootblower jet

In this study, FEM was implemented using ABAQUS/Explicit to simulate the sootblower jet dynamics and deposit failure. The type of sootblower selected in this study was the IR-3Z developed by the Diamond-Power Company, USA. Fig. 2 displays the

diagrammatic sketch of the model, in which a wall tube and its slag deposit on the surface along with the sootblower jet nozzle are emphasized. Table 1 lists other relevant parameters of the object model. The distance between the sootblower jet nozzle and the deposit was set as 78 mm in this model.

Fig. 4 shows the insertion of zero-thickness cohesive elements among the adjacent solid elements in the deposit model. Cracks can initiate and extend these inserting elements when the maximum nominal stress criterion is satisfied.

Table 1 Relevant parameters used in the model

Parameter	Value
External diameter of jet (mm)	30
Internal diameter of jet (mm)	25.4
Length of sootblower jet (mm)	100
External diameter of wall tube (mm)	60
Internal diameter of wall tube (mm)	50
Height of wall tube (mm)	200
Thickness of deposit (mm)	4

(a)   (b)
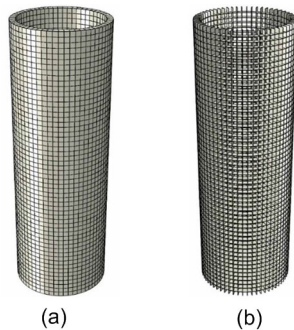
Fig. 4 Numerical model for deposit cracking: (a) deposit model; (b) embedded cohesive elements

The most important property concerning ash deposit removal is the tensile strength because deposits can break at their weakest point (Zbogar et al., 2009). Moreover, the tensile strength of the deposits is influenced by the deposit chemical composition, thickness, and porosity (Kaliazine et al., 1997). In this study, the tensile strength of the ash deposit was assumed as that corresponding to the onset of damage stress, t^o, mentioned in the CZM because deposit damage was assumed to initiate when the stress on the deposit surface was greater than the tensile strength. Elastic properties are also relevant for deposit be-

havior, including Poisson's ratio and the elastic (Young's) modulus. For Poisson's ratio, the value range of 0.20–0.25 was acceptable in this study, similar to the range of most types of glass and ceramic (Wain et al., 1991). The elastic (Young's) modulus presents the relative stiffness within the elastic range (Zbogar et al., 2009), and it determines the initially linear elastic behavior with nominal stress and strain quantities in the traction–separation curve. The elastic modulus of porous-like material deposits (E) can be related to the elastic modulus of nonporous materials (Wain et al., 1991) via the Mackenzie relationship (developed for ceramic porous materials):

$$E = E_0(1 - ap + bp^2), \qquad (7)$$

where E_0 represents the elastic modulus of nonporous materials, p is the porosity of porous materials, and a and b are the pore shape factors of porous materials.

The parameters of the CZM included Young's modulus (E), tensile strength (t^o), and failure displacement (δ^f). Previous studies (Kaliazine et al., 1997; Zbogar et al., 2009) have shown that the tensile strength and Young's modulus of the ash deposits depend strongly on the deposit porosity. The porosity of a typical coal deposit is 20%, and the tensile strength and Young's modulus were obtained according to their relationships with porosity as reported in the literature (Kaliazine et al., 1997; Zbogar et al., 2009). Failure displacement (δ^f) was calculated by means of Eq. (6) according to Guo (2014); the results are listed in Table 2. The most common material of boiler wall tubes is low-carbon steel (such as No. 20 steel), whose properties are also included in Table 2.

The properties of the sootblower steam material were modeled using the U_s–U_p equation of state materials in ABAQUS. This equation is also called the Mie–Grüneisen equation, and it describes the linear relationship between shock and particle velocities, as follows:

$$U_s = c_0 + sU_p, \qquad (8)$$

where U_s is the shock velocity, U_p is the particle velocity, c_0 denotes the speed of sound in the fluid material, and s is the material constant (Smojver and

Ivančević, 2011). The relationship between pressure p and density ρ can be defined as (ABAQUS, 2016)

$$p = \frac{\rho_0 c_0^2 \eta}{(1-s\eta)^2}\left(1 - \frac{\Gamma_0 \eta}{2}\right) + \Gamma_0 \rho_0 E_m, \qquad (9)$$

where ρ_0 represents the initial material density, $\eta = 1-\rho_0/\rho$ is the nominal volumetric compressive strain, Γ_0 is the material constant, and E_m is the internal energy per unit mass (Smojver and Ivančević, 2011). Parameters s and Γ_0 are set to zero to provide a simple hydrostatic bulk response (Chizari et al., 2009). The main properties of steam are as follows: density, ρ_0=1.46 kg/m^3; steam temperature, T=600 K; working pressure of steam, P_0=0.4 MPa; acoustic speed in the material, c_0=597 m/s.

Table 2 Properties of the deposit and wall tube adopted in simulation (Kaliazine et al., 1997; Zbogar et al., 2009; Guo, 2014)

Property	Value	
	Deposit	Wall tube
Density, ρ (kg/m^3)	2700	7900
Young's modulus, E (MPa)	1.0×10^4	7.9×10^5
Poisson's ratio, v	0.25	0.3
Porosity (%)	20	–
Tensile strength, t (MPa)	5	–

4 Results and discussion

4.1 Mesh independence analysis

The mesh accuracy of the deposit model is an important factor in determining the correctness of the simulation results, including the shape of cracks and failure time of the deposit. Although a fine deposit mesh can enhance the rationality and precision of the concerned modeling, the calculating time can also increase.

The scalar stiffness degradation variable D, as described in Eqs. (3) and (4), was adopted in this study to measure mesh independence. Fig. 1 illustrates the significance of D. After ABAQUS completed the calculations, the output database files were post-processed to extract the number of damaged cohesive elements from each output dataset of the deposit model. In addition, deposit zones were considered entirely damaged if the value of D was over 0.9 in cohesive elements. The fracture of the cohesive

elements became increasingly severe as the value of D approached 1. The destructive degree of the deposit model can be defined as

$$\eta_t = \frac{N_t^{0.9}}{N_{\text{total}}}\times100\%, \qquad (10)$$

where $N_t^{0.9}$ denotes the number of cohesive elements whose value of D exceeds 0.9 at time t; N_{total} is the sum of the number of cohesive elements, which is a constant number if the cohesive elements are embedded into the deposit model; η_t is the parameter that measures the destructive degree of the deposit at time t. Therefore, the closer the value of η_t is to 100%, the more severe is the damage degree in the deposit model.

In mesh dependency analysis, three different mesh sizes (i.e. coarse, middle, and fine meshes with 3318, 6667, and 9044 cohesive elements, respectively) were compared via the value of η_t, which changes with the simulation time (1.5 ms). In addition, the value of the sootblowing pressure was assumed as 1.2 MPa in the three cases, as shown in Fig. 5. We note that the η_t–time curve trends with middle and fine meshes are roughly similar. In comparison with the cases of the middle and fine meshes, the deposit with the coarse mesh is easily destroyed and breaks entirely at 1 ms. Meanwhile, approximately 80% of the middle and fine cases are observed to be destroyed simultaneously. However, the elements contained in the coarse mesh can be easily distorted excessively upon high-temperature steam impact, which leads to non-convergence of the results. In view of the calculating time cost, convergence, and mesh precision, the middle mesh size was selected in this study.
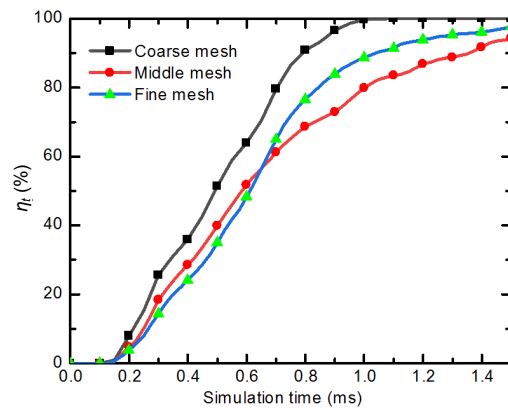
Fig. 5 Mesh dependency analysis of three different sizes of deposit mesh (steam pressure is 1.2 MPa)
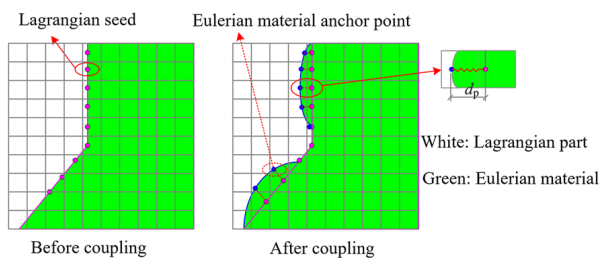
4.2 Sootblower steam flow and deposit-breaking process

To describe the contact at the interface between the Eulerian and Lagrangian domains, we used the penalty method in ABAQUS. Seeds were created at the Lagrangian element edges and faces while anchor points were created on the Eulerian material surface (Benson and Okazawa, 2004; Qiu et al., 2011). The penalty method allowed small penetration of the Eulerian material into the Lagrangian domain, as shown in Fig. 6. Contact force F_p, which was enforced between the seeds and anchor points, was proportional to penetration distance d_p, as expressed in Eq. (11):
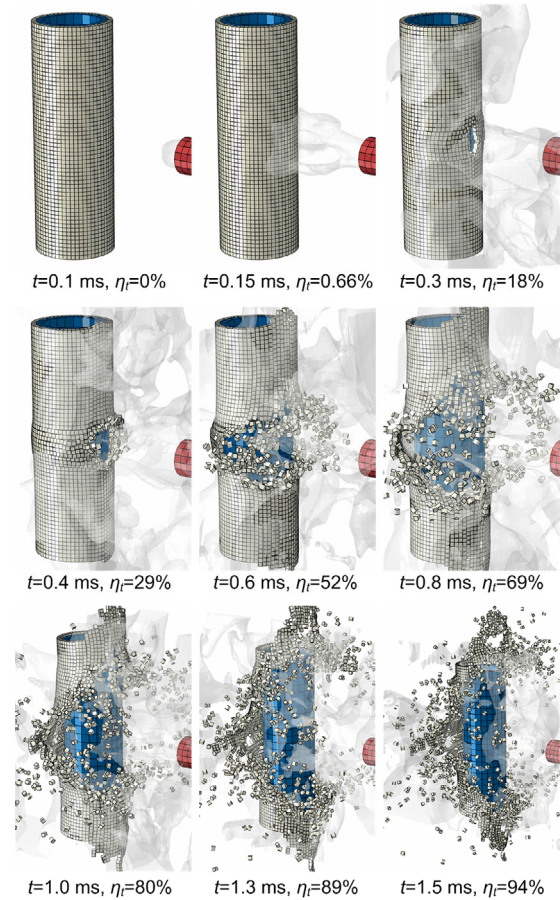
$$F_p = k_p d_p, \tag{11}$$

where the factor k_p denotes the penalty stiffness that depends on the Lagrangian and Eulerian material properties. Contact force F_p was regarded as the compressive force impressed on the deposit from the steam jet.

Deposit failure and chip formation during deposit breaking by steam flow sootblowing were simulated at a sootblowing pressure of 1.2 MPa. The interval time between output images was 0.05 ms, and the total simulation time was 1.5 ms, which was sufficient to express the details of the deposit changes. The failure time of the deposit coincided with certain research results (Pophali et al., 2013). Fig. 7 illustrates the dynamic results of the deposit-cracking process during sootblowing, including variations in the high-pressure steam flow, fracture zone of the deposit, and values of η_t. Fig. 8 reveals the D values of the cohesive elements inserted to observe their dynamic changes during the simulation.
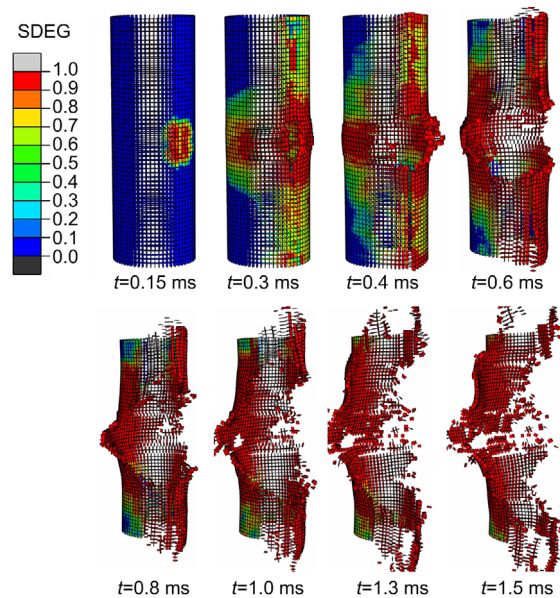

Fig. 7 Dynamic results during sootblowing processes

$t=0.1$ ms, $\eta_t=0\%$ $t=0.15$ ms, $\eta_t=0.66\%$ $t=0.3$ ms, $\eta_t=18\%$

$t=0.4$ ms, $\eta_t=29\%$ $t=0.6$ ms, $\eta_t=52\%$ $t=0.8$ ms, $\eta_t=69\%$

$t=1.0$ ms, $\eta_t=80\%$ $t=1.3$ ms, $\eta_t=89\%$ $t=1.5$ ms, $\eta_t=94\%$

$t=0.15$ ms $t=0.3$ ms $t=0.4$ ms $t=0.6$ ms

$t=0.8$ ms $t=1.0$ ms $t=1.3$ ms $t=1.5$ ms

Fig. 8 Value of scalar stiffness degradation variable (SDEG, *D*) of inserted cohesive elements at different times
Note: for interpretation of the references to color in this figure, the reader is referred to the web version of this article



Fig. 6 Definitions corresponding to penalty method
Note: for interpretation of the references to color in this figure, the reader is referred to the web version of this article

As shown in Fig. 7, the steam flow is translucent. This result is in accordance with practical scenarios, and it is beneficial to investigate the overall process of crack formation directly. The steam flow ejected from the sootblower nozzle can be observed when the time is 0.1 ms. In the next 0.05 ms, the steam flow immediately interacts with the deposit layer. The initiation of microscopic cracks in the deposit zone under steam pressure is observed at 0.3 ms, and the value of η_t reaches 18% at this time. Corresponding to the same time instant in Fig. 8, the cohesive elements of the deposit/steam contact area are already destroyed, and the stress wave gradually spreads at 0.3 ms. The area of the destroyed deposit presents a rapid growth at 0.4 ms, and the maximum amount of deposit is ruptured at 1 ms, with the value of η_t reaching 80%. The steam flow gradually diffuses the entire Eulerian domain modeled previously, and when the jet contacts the brittle deposit, it shatters the deposit into pieces. As shown in Fig. 8, the red area of the cohesive elements indicate severe deposit damage, and the damaged deposit area slightly changes from 1.0 ms to 1.5 ms. The reverse sides of the deposit near the edge cannot easily be compressed and wrecked under steam impact. The value of η_t reaches 94% at the end of the simulation. Therefore, nearly all areas in the deposit model are destroyed.

In this study, the deposit material properties were independent of the microstructure details and considered as isotropic. The sootblowing jet imposed a large compressive force on the deposit when it impacted the surface of the deposit, and subsequently, the deposit elements were squeezed and deformed in the transverse direction. Transverse deformation produced transverse normal tension on the cohesive elements, and cracks occurred when the normal tension was greater than the tensile strength (t^o).

Fig. 9 shows the calculated fracture rate of ash deposit, $d\eta_t/dt$. The figure also presents the onsite fracture time of five equidistant points (A, B, C, D, and E) on the deposit surface. When the initial pit is formed at point A due to jet impingement, a transverse normal tension is simultaneously generated. Thereafter, the tension wave spreads quickly in the deposit from point A, which leads to acceleration of the fracture rate accompanied with the sootblowing jet impact, as implied by the right-hand portion of the $d\eta_t/dt$ curve from point A to point C. After the rate

reaches the peak at 0.4 ms, over 50% of deposit is broken, and the fracture rate begins decreasing because the rear portion of the deposit is not directly impacted by the steam jet, as indicated in the curve from point C to point E. The deposit is finally broken at E without steam impact due to stress wave propagation. In summary, the spread of the transverse normal tension caused by the steam jet primarily contributes to the deposit fracture, and further, direct steam impact on the deposit forms the initial source of transverse normal tension and plays a subsidiary role after initiation of the deposit fracture.
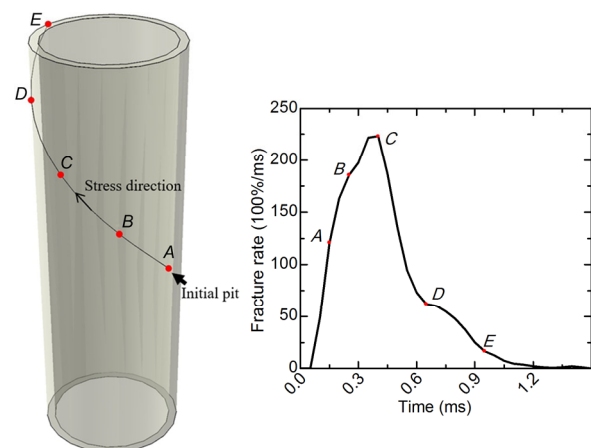
Fig. 9 Fracture rate of points of interest on deposit under 1.8-MPa steam pressure

4.3 Effect of different sootblowing pressures on deposit failure

Sootblowing pressure is an essential parameter for this simulation, and high sootblowing pressure can easily destroy the deposit. High-pressure steam can also erode the wall tube surface and consume additional steam. Hence, the extent of deposit fracture was compared through η_t–time curves under different sootblowing pressures, as shown in Fig. 10. Under different sootblowing pressures of 0.9–1.8 MPa, sootblowing yields different dynamic features of deposit failure. Although the results of deposit failure show similar tendencies, high sootblowing pressures lead to rapid deposit cracking. The deposit fails at 1 ms when the sootblowing pressure is 1.8 MPa. However, deposit failure occurs slowly at the pressure of 0.9 MPa, and a long sootblowing time of over 1.4 ms is necessary. The η_t–time curves nearly coincide for

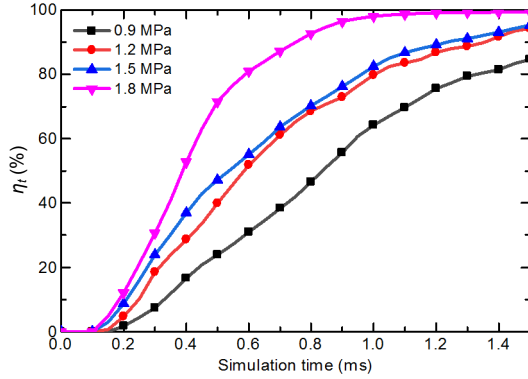pressures of 1.5 MPa and 1.2 MPa, which implies similar deposit failure dynamics.

Fig. 10 Extent of deposit failure under different sootblowing pressures

Wall tube steel can be exposed to high-pressure sootblowing steam if the slag deposit is broken and falls off, thereby adversely affecting steel safety and its lifetime. Wall tube leaks may also occur. Thus, the wall tube stress due to sootblowing (SWS) was examined to evaluate the effects of sootblowing on the steel lifetime. Therefore, the maximum SWS (MSWS) on the windward side was calculated as shown in Fig. 11. Another parameter concerning sootblowing is steam consumption, which is closely related to economic benefits. Therefore, the mass of steam consumption per wall tube surface, V, was adopted, which can be expressed as

$$V = v_{avg} \cdot t_{\eta 80\%} \cdot \rho_{steam} \cdot \frac{S_{jet}}{S_{tube}}, \qquad (12)$$

where v_{avg} denotes the average entrance velocity of sootblowing steam flow, $t_{\eta 80\%}$ is the sootblowing time corresponding to η_t=80%, ρ_{steam} is the density of steam, S_{jet} is the exit area of the sootblower nozzle jet, and S_{tube} is the area of the wall tube surface.

As shown in Fig. 11, the MSWS steadily increases with the sootblowing pressure. However, steam consumption costs fluctuate with the pressure. Although steam consumption is the least when the sootblowing pressure is 1.8 MPa, the MSWS reaches about 24 MPa during sootblowing, which can cause serious material erosion. In contrast, MSWS is the lowest when the sootblower pressure is 0.9 MPa; however,

more steam is consumed than that in the high-pressure cases. Given that the steam jets at 1.2 MPa and 1.5 MPa achieve similar deposit failures, the 1.2-MPa steam pressure is selected upon considering the factors of MSWS and V. When the pressure value of 1.2 MPa is adopted, MSWS is approximately 13 MPa, V is 0.14 kg/m², and the necessary sootblowing time is 1.1 ms. Therefore, this set of sootblowing parameters was suitable and economical for boiler operation.
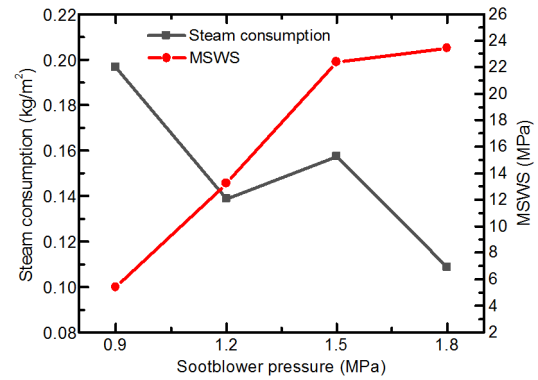

Fig. 11 Steam consumption and MSWS under various sootblower pressures

5 Conclusions

To replicate the dynamic failure of ash deposit under steam sootblowing, we developed a novel numerical model of deposit and steam flow in ABAQUS through CZM and CEL analysis. The dynamic details and mechanism of deposit failure by steam sootblowing were revealed by the proposed model. The destructive degree of the deposit and the scalar stiffness degradation variable were obtained to measure the dynamic destructive status during sootblowing. The fracture mechanism was revealed by fracture rate analysis of the ash deposit. The spread of transverse normal tension caused by steam jets was the primary contributor to deposit fracture, and direct steam impact on the deposit formed the initial source of transverse normal tension, which played a subsidiary role after initiation of the deposit fracture.

The effects of the sootblowing pressure on the deposit were studied contrastively in the range of 0.9–1.8 MPa. The damage degree of deposit, steam consumption, and MSWS were chosen as representative effects of the sootblowing pressure. In general,

the deposit began to break nearly simultaneously for all pressures, and subsequently, the breaking process firstly presented an accelerated tendency followed by a decelerated one. Higher sootblowing pressure led to quicker deposit fracture, and the deposit failure was complete over 1.0–1.5 ms due to different pressures. The simulation results indicated that the sootblowing pressure of 1.2 MPa was suitable and economical for boiler/furnace operation.

References

ABAQUS, 2016. ABAQUS Analysis User's Manual. Dassault Systèmes Simulia Corp, Johnston, Rhode Island, USA.

Awinda K, Chen JY, Barnett SJ, 2016. Investigating geometrical size effect on the flexural strength of the ultra high performance fibre reinforced concrete using the cohesive crack model. *Construction and Building Materials*, 105: 123-131.
https://doi.org/10.1016/j.conbuildmat.2015.12.012

Benson DJ, Okazawa S, 2004. Contact in a multi-material Eulerian finite element formulation. *Computer Methods in Applied Mechanics and Engineering*, 193(39-41): 4277-4298.
https://doi.org/10.1016/j.cma.2003.12.061

Bussmann M, Emami B, Tandra D, et al., 2013. Modeling of sootblower jets and the impact on deposit removal in industrial boilers. *Energy & Fuels*, 27(10):5733-5737.
https://doi.org/10.1021/ef400783d

Camanho PP, Dávila CG, 2002. Mixed-mode Decohesion Finite Elements for the Simulation of Delamination in Composite Materials. NASA/TM-2002-211737, National Aeronautics and Space Administration, Langley Research Center, Hampton, USA, p.1-37.

Chen JY, Ravey E, Hallett S, et al., 2009. Prediction of delamination in braided composite T-piece specimens. *Composites Science and Technology*, 69(14):2363-2367.
https://doi.org/10.1016/j.compscitech.2009.01.027

Chizari M, Barrett LM, Al-Hassani STS, 2009. An explicit numerical modelling of the water jet tube forming. *Computational Materials Science*, 45(2):378-384.
https://doi.org/10.1016/j.commatsci.2008.10.012

Doroudi S, Pophali A, Bussmann M, et al., 2014. Modelling sootblower jet effectiveness with ANSYS fluent. *Journal of Science & Technology for Forest Products and Processes*, 4(4):30-35.

Ebrahimi-Sabet SA, 2001. A Laboratory Study of Deposit Removal by Debonding and Its Application to Fireside Deposits in Kraft Recovery Boilers. PhD Thesis, University of Toronto, Toronto, Canada.

Elices M, Guinea GV, Gómez J, et al., 2002. The cohesive zone model: advantages, limitations and challenges. *Engineering Fracture Mechanics*, 69(2):137-163.
https://doi.org/10.1016/S0013-7944(01)00083-2

Fan JR, Zha XD, Sun P, et al., 2001. Simulation of ash deposit in a pulverized coal-fired boiler. *Fuel*, 80(5):645-654.
https://doi.org/10.1016/S0016-2361(00)00134-4

Gálvez JC, Červenka J, Cendón DA, et al., 2002. A discrete crack approach to normal/shear cracking of concrete. *Cement and Concrete Research*, 32(10):1567-1585.
https://doi.org/10.1016/S0008-8846(02)00825-6

Griffith AA, 1921. VI. The phenomena of rupture and flow in solids. *Philosophical Transactions of the Royal Society of London Series A, Containing Papers of a Mathematical or Physical Character*, 221(582-593):163-198.

Gui Y, Bui HH, Kodikara J, 2015. An application of a cohesive fracture model combining compression, tension and shear in soft rocks. *Computers and Geotechnics*, 66:142-157.
https://doi.org/10.1016/j.compgeo.2015.01.018

Gui Y, Bui HH, Kodikara J, et al., 2016. Modelling the dynamic failure of brittle rocks using a hybrid continuum-discrete element method with a mixed-mode cohesive fracture model. *International Journal of Impact Engineering*, 87:146-155.
https://doi.org/10.1016/j.ijimpeng.2015.04.010

Guo LW, 2014. Development of a Three-dimensional Fracture Model for the Combined Finite-discrete Element Method. PhD Thesis, Imperial College London, London, UK.

Guo LW, Xiang JS, Latham JP, et al., 2016. A numerical investigation of mesh sensitivity for a new three-dimensional fracture model within the combined finite-discrete element method. *Engineering Fracture Mechanics*, 151:70-91.
https://doi.org/10.1016/j.engfracmech.2015.11.006

Hillerborg A, Modéer M, Petersson PE, 1976. Analysis of crack formation and crack growth in concrete by means of fracture mechanics and finite elements. *Cement and Concrete Research*, 6(6):773-781.
https://doi.org/10.1016/0008-8846(76)90007-7

Jameel MI, Cormack DE, Tran HN, et al., 1994. Sootblower optimization-part 1: fundamental hydrodynamics of a sootblower nozzle and jet. *TAPPI Journal*, 77(5):135-142.

Jiang HX, Meng DG, 2018. 3D numerical modelling of rock fracture with a hybrid finite and cohesive element method. *Engineering Fracture Mechanics*, 199:280-293.
https://doi.org/10.1016/j.engfracmech.2018.05.037

Kaliazine AL, Piroozmand F, Cormack DE, et al., 1997. Sootblower optimization II: deposit and sootblower interaction. *TAPPI Journal*, 80(11):201-208.

Kaliazine AL, Cormack DE, Ebrahimi-Sabet A, et al., 1999. The mechanics of deposit removal in kraft recovery boilers. *Journal of Pulp and Paper Science*, 25(12):418-424.

Kazerani T, Yang ZY, Zhao J, 2012. A discrete element model for predicting shear strength and degradation of rock joint by using compressive and tensile test data. *Rock Mechanics and Rock Engineering*, 45(5):695-709.
https://doi.org/10.1007/s00603-011-0153-6

May M, 2015. Numerical evaluation of cohesive zone models

for modeling impact induced delamination in composite materials. *Composite Structures*, 133:16-21.
https://doi.org/10.1016/j.compstruct.2015.07.032

Pophali A, Eslamian M, Kaliazine A, et al., 2009. Breakup mechanisms of brittle deposits in kraft recovery boilers–a fundamental study. *TAPPI Journal*, 8(9):4-9.

Pophali A, Emami B, Bussmann M, et al., 2013. Studies on sootblower jet dynamics and ash deposit removal in industrial boilers. *Fuel Processing Technology*, 105:69-76.
https://doi.org/10.1016/j.fuproc.2011.04.034

Qiu G, Henke S, Grabe J, 2011. Application of a coupled Eulerian–Lagrangian approach on geomechanical problems involving large deformations. *Computers and Geotechnics*, 38(1):30-39.
https://doi.org/10.1016/j.compgeo.2010.09.002

Smojver I, Ivančević D, 2011. Bird strike damage analysis in aircraft structures using Abaqus/Explicit and coupled Eulerian Lagrangian approach. *Composites Science and Technology*, 71(4):489-498.
https://doi.org/10.1016/j.compscitech.2010.12.024

Su XT, Yang ZJ, Liu GH, 2010a. Finite element modelling of complex 3D static and dynamic crack propagation by embedding cohesive elements in Abaqus. *Acta Mechanica Solida Sinica*, 23(3):271-282.
https://doi.org/10.1016/S0894-9166(10)60030-4

Su XT, Yang ZJ, Liu GH, 2010b. Monte Carlo simulation of complex cohesive fracture in random heterogeneous quasi-brittle materials: a 3D study. *International Journal of Solids and Structures*, 47(17):2336-2345.
https://doi.org/10.1016/j.ijsolstr.2010.04.031

Turon A, Dávila CG, Camanho PP, et al., 2007. An engineering solution for mesh size effects in the simulation of delamination using cohesive zone models. *Engineering Fracture Mechanics*, 74(10):1665-1682.
https://doi.org/10.1016/j.engfracmech.2006.08.025

Wain SE, Livingston WR, Sanyal A, et al., 1991. Thermal and mechanical properties of boiler slags of relevance to sootblowing. Proceedings of the Engineering Foundation Conference on Inorganic Transformations and Ash Deposition During Combustion, p.459-470.

Yao Y, 2012. Linear elastic and cohesive fracture analysis to model hydraulic fracture in brittle and ductile rocks. *Rock Mechanics and Rock Engineering*, 45(3):375-387.

https://doi.org/10.1007/s00603-011-0211-0

Žbogar A, Jensen PA, Frandsen FJ, et al., 2006. Experimental investigation of ash deposit shedding in a straw-fired boiler. *Energy & Fuels*, 20(2):512-519.
https://doi.org/10.1021/ef050037a

Zbogar A, Frandsen F, Jensen PA, et al., 2009. Shedding of ash deposits. *Progress in Energy and Combustion Science*, 35(1):31-56.
https://doi.org/10.1016/j.pecs.2008.07.001

中文概要

题　目：蒸汽吹灰过程中水冷壁渣层破坏过程的模拟分析

目　的：蒸汽吹灰是锅炉运行中常见的破坏水冷壁渣层的方法。本文通过建立三维吹灰模型，模拟不同压力下吹灰过程中蒸汽射流和渣层破坏的动态变化过程，研究在渣层破坏过程中应力波的传播变化，得出条件合适的吹灰参数。

创新点：1. 通过内聚力单元法和耦合欧拉-拉格朗日法建立吹灰流程的三维数值模型，详细揭示渣层破坏的动力学过程，并对蒸汽射流的扩散和应力波在渣层中的传播进行全过程分析；2. 通过建立三维数值模拟，研究吹灰蒸汽压力对渣层破坏、管壁应力和蒸汽消耗的影响，并通过模拟结果探讨合适的吹灰参数。

方　法：1. 对渣层模型采用内聚力单元法进行建模；2. 对蒸汽射流和渣层的流固耦合现象采用 ABAQUS 中的耦合欧拉-拉格朗日法进行分析。

结　论：1. 越高的吹灰压力会导致渣层被破坏得越快并最终完全脱离水冷壁；综合考虑渣层破坏效率、水冷壁管应力和蒸汽消耗的影响，1.2 MPa 是最合适和经济的吹灰压力参数。2. 蒸汽射流带来的切向应力是引起渣层破坏的主要因素，射流对渣层的直接冲击是切向应力的来源，并且是渣层破坏的次要因素。

关键词：吹灰；锅炉；数值模型；内聚力单元法；渣层破坏